

## Observation of topologically protected Dirac spin-textures and $\pi$ Berry's phase in pure Antimony (Sb) and topological insulator BiSb

D. Hsieh,<sup>1</sup> Y. Xia,<sup>1</sup> L. Wray,<sup>1</sup> D. Qian,<sup>1</sup> A. Pal,<sup>1</sup> J. H. Dil,<sup>2,3</sup> F. Meier,<sup>2,3</sup> J. Osterwalder,<sup>3</sup> G. Bihlmayer,<sup>4</sup> C. L. Kane,<sup>5</sup> Y. S. Hor,<sup>6</sup> R. J. Cava,<sup>6</sup> and M. Z. Hasan<sup>1,7</sup>

<sup>1</sup>Joseph Henry Laboratories of Physics, Princeton University, Princeton, NJ 08544, USA

<sup>2</sup>Swiss Light Source, Paul Scherrer Institute, CH-5232, Villigen, Switzerland

<sup>3</sup>Physik-Institut, Universität Zürich-Irchel, 8057 Zürich, Switzerland

<sup>4</sup>Institut für Festkörperforschung, Forschungszentrum Jülich, D-52425 Jülich, Germany

<sup>5</sup>Department of Physics and Astronomy, University of Pennsylvania, Philadelphia, PA 19104, USA

<sup>6</sup>Department of Chemistry, Princeton University, Princeton, NJ 08544, USA

<sup>7</sup>Princeton Center for Complex Materials, Princeton University, Princeton, NJ 08544, USA\*

(Dated: November 8, 2018)

A topologically ordered material is characterized by a rare quantum organization of electrons that evades the conventional spontaneously broken symmetry based classification of condensed matter. Exotic spin transport phenomena such as the dissipationless quantum spin Hall effect have been speculated to originate from a novel topological order whose identification requires a spin sensitive measurement. Using *spin-resolved ARPES*, we probe the spin degrees of freedom and demonstrate that topological quantum numbers are uniquely determined from spin texture imaging measurements. Applying this method to pure antimony (Sb) and  $\text{Bi}_{1-x}\text{Sb}_x$ , we identify the origin of its novel order and unusual chiral topological properties. These results taken together constitute the observation of surface electrons collectively carrying a geometrical quantum (Berry's) phase and definite chirality in pure Antimony, Sb, and topological insulator BiSb, which are the key electronic properties for realizing topological quantum computing via the Majorana fermion framework. This paper contains the details of our previously reported (first reported in Science **323**, 919 (2009)) observation of a negative mirror Chern quantum number for pure Sb.

PACS numbers:

Ordered phases of matter such as a superfluid or a ferromagnet are usually associated with the breaking of a symmetry and are characterized by a local order parameter [1], and the typical experimental probes of these systems are sensitive to order parameters. The discovery of the quantum Hall effects in the 1980s revealed a new and rare type of order that is derived from an organized collective quantum motion of electrons [2-4]. These so-called "topologically ordered phases" do not exhibit any symmetry breaking and are characterized by a topological number [5] as opposed to a local order parameter. The classic experimental probe of topological quantum numbers is magneto-transport, where measurements of the quantization of Hall conductivity  $\sigma_{xy} = ne^2/h$  (where  $e$  is the electric charge and  $h$  is Planck's constant) reveals the value of the topological number  $n$  that characterizes the quantum Hall effect state [6].

Recent theoretical and experimental studies suggest that a new class of quantum Hall-like topological phases can exist in spin-orbit materials without external magnetic fields, with interest centering on two examples, the "quantum spin Hall insulator" [7-9] and the "strong topological insulator" [10,11]. Their topological order is believed to give rise to unconventional spin physics at the

sample edges or surfaces with potential applications ranging from dissipationless spin currents [12] to topological (fault-tolerant) quantum computing [13]. However, unlike conventional quantum Hall systems, these novel topological phases do not necessarily exhibit a quantized charge or spin response ( $\sigma_{xy} \neq ne^2/h$ ) [14,15]. In fact, the spin polarization is not a conserved quantity in a spin-orbit material. Thus, their topological quantum numbers, the analogues of  $n$ , cannot be measured via the classic von Klitzing-type [2] transport methods.

Here we show that spin-resolved angle-resolved photoemission spectroscopy (spin-ARPES) can perform analogous measurements for topological metals and insulators. We measured all of the topological numbers for  $\text{Bi}_{1-x}\text{Sb}_x$  and provide an identification of its spin-texture, which heretofore was unmeasured despite its surface states having been observed [10]. The measured spin texture reveals the existence of a non-zero geometrical quantum phase (Berry's phase [16,17]) and the handedness or chiral properties. More importantly, this technique enables us to investigate aspects of the metallic regime of the  $\text{Bi}_{1-x}\text{Sb}_x$  series, such as spin properties in pure Sb, which are necessary to determine the microscopic origin of topological order. Our measurements on pure metallic Sb show that its surface carries a geometrical (Berry's) phase and chirality property unlike the conventional spin-orbit metals such as gold (Au), which has zero net Berry's phase and no net chirality [18].

\*Electronic address: mzhasan@Princeton.edu

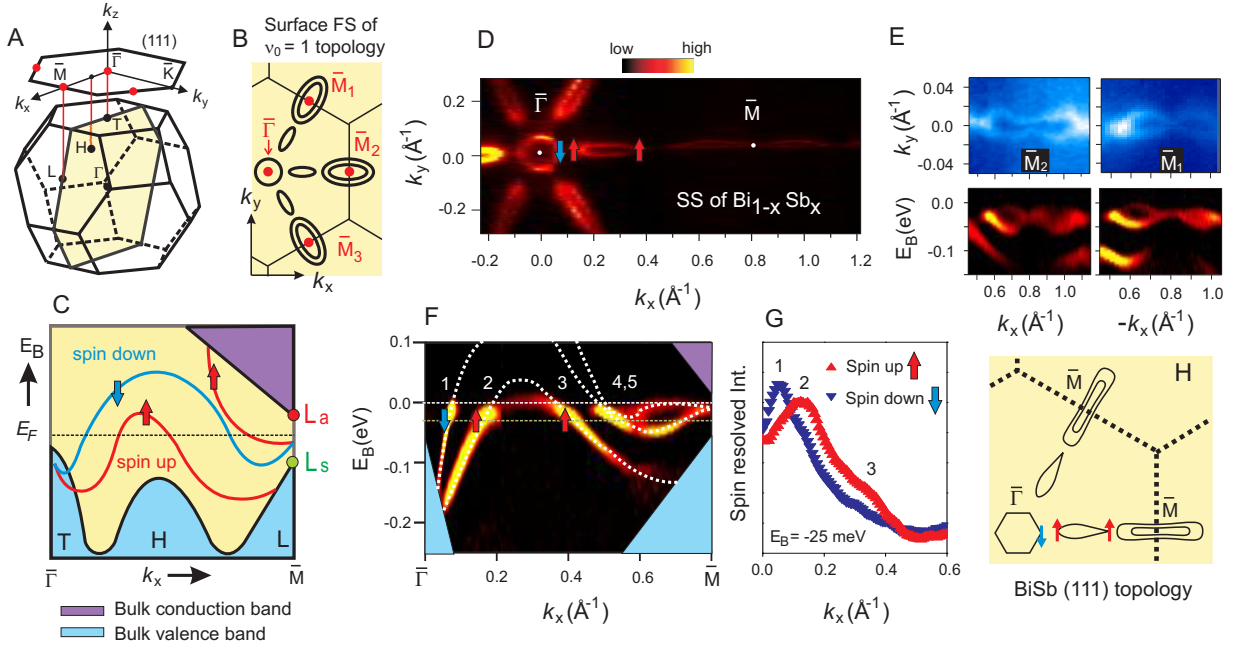


FIG. 1: Spin-texture and  $\pi$  Berry's Phase in BiSb

Strong topological materials are distinguished from ordinary materials such as gold by a topological quantum number,  $\nu_0 = 1$  or  $0$  respectively [14,15]. For  $\text{Bi}_{1-x}\text{Sb}_x$ , theory has shown that  $\nu_0$  is determined solely by the character of the bulk electronic wave functions at the  $L$  point in the three-dimensional (3D) Brillouin zone (BZ). When the lowest energy conduction band state is composed of an antisymmetric combination of atomic  $p$ -type orbitals ( $L_a$ ) and the highest energy valence band state is composed of a symmetric combination ( $L_s$ ), then  $\nu_0 = 1$ , and vice versa for  $\nu_0 = 0$  [11]. Although the bonding nature (parity) of the states at  $L$  is not revealed in a measurement of the bulk band structure, the value of  $\nu_0$  can be determined from the spin-textures of the surface bands that form when the bulk is terminated. In particular, a  $\nu_0 = 1$  topology requires the terminated surface to have a Fermi surface (FS) [1] that supports a non-zero Berry's phase (odd as opposed to even multiple of  $\pi$ ), which is not realizable in an ordinary spin-orbit material.

In a general inversion symmetric spin-orbit insulator, the bulk states are spin degenerate because of a combination of space inversion symmetry [ $E(\vec{k}, \uparrow) = E(-\vec{k}, \uparrow)$ ] and time reversal symmetry [ $E(\vec{k}, \uparrow) = E(-\vec{k}, \downarrow)$ ]. Because space inversion symmetry is broken at the terminated surface, the spin degeneracy of surface bands can be lifted by the spin-orbit interaction [19-21]. However, according to Kramers theorem [16], they must remain spin degenerate at four special time reversal invariant momenta ( $\vec{k}_T = \bar{\Gamma}, \bar{M}$ ) in the surface BZ [11], which for the (111) surface of  $\text{Bi}_{1-x}\text{Sb}_x$  are located at  $\bar{\Gamma}$  and three equivalent  $\bar{M}$  points [see Fig.1(A)].

Depending on whether  $\nu_0$  equals 0 or 1, the Fermi sur-

face pockets formed by the surface bands will enclose the four  $\vec{k}_T$  an even or odd number of times respectively. If a Fermi surface pocket does not enclose  $\vec{k}_T$  ( $= \bar{\Gamma}, \bar{M}$ ), it is irrelevant for the topology [11,20]. Because the wave function of a single electron spin acquires a geometric phase factor of  $\pi$  [16] as it evolves by  $360^\circ$  in momentum space along a Fermi contour enclosing a  $\vec{k}_T$ , an odd number of Fermi pockets enclosing  $\vec{k}_T$  in total implies a  $\pi$  geometrical (Berry's) phase [11]. In order to realize a  $\pi$  Berry's phase the surface bands must be spin-polarized and exhibit a partner switching [11] dispersion behavior between a pair of  $\vec{k}_T$ . This means that any pair of spin-polarized surface bands that are degenerate at  $\bar{\Gamma}$  must not re-connect at  $\bar{M}$ , or must separately connect to the bulk valence and conduction band in between  $\bar{\Gamma}$  and  $\bar{M}$ . The partner switching behavior is realized in Fig. 1(C) because the spin down band connects to and is degenerate with different spin up bands at  $\bar{\Gamma}$  and  $\bar{M}$ . The partner switching behavior is realized in Fig. 2(A) because the spin up and spin down bands emerging from  $\bar{\Gamma}$  separately merge into the bulk valence and conduction bands respectively between  $\bar{\Gamma}$  and  $\bar{M}$ .

We first investigate the spin properties of the topological insulator phase. Spin-integrated ARPES [19] intensity maps of the (111) surface states of insulating  $\text{Bi}_{1-x}\text{Sb}_x$  taken at the Fermi level ( $E_F$ ) [Figs 1(D)&(E)] show that a hexagonal FS encloses  $\bar{\Gamma}$ , while dumbbell shaped FS pockets that are much weaker in intensity enclose  $\bar{M}$ . By examining the surface band dispersion below the Fermi level [Fig.1(F)] it is clear that the central hexagonal FS is formed by a single band (Fermi crossing 1) whereas the dumbbell shaped FSs are formed by the

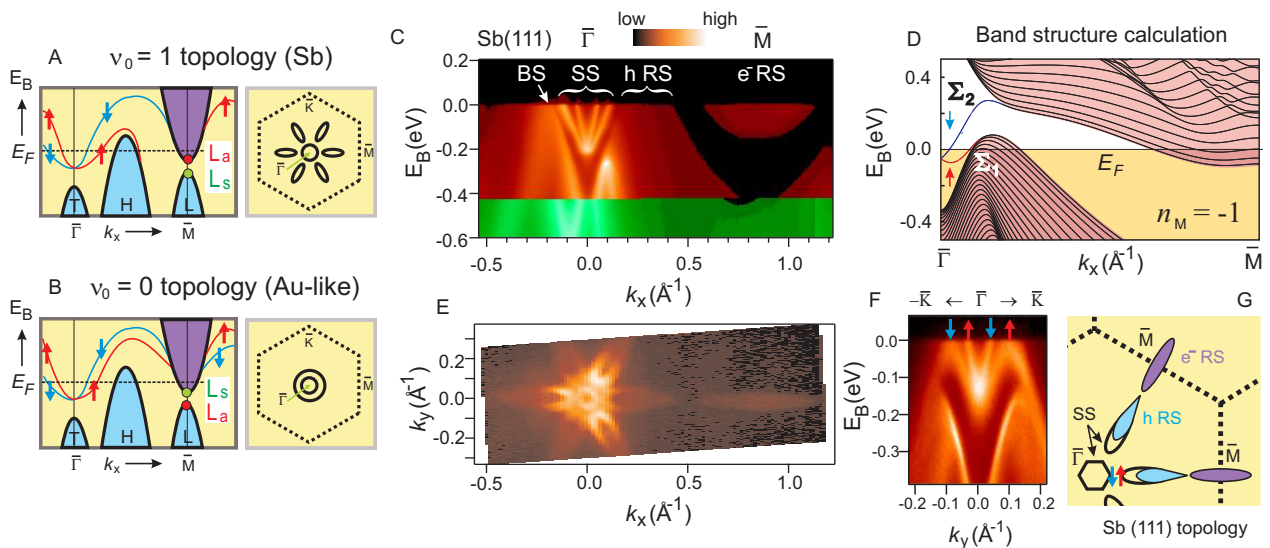


FIG. 2: Topological nature of the surface states in pure Sb (Antimony)

merger of two bands (Fermi crossings 4 and 5) [10].

This band dispersion resembles the partner switching dispersion behavior characteristic of topological insulators. To check this scenario and determine the topological index  $\nu_0$ , we have carried out spin-resolved photoemission spectroscopy. Fig.1(G) shows a spin-resolved momentum distribution curve taken along the  $\bar{\Gamma}$ - $\bar{M}$  direction at a binding energy  $E_B = -25$  meV [Fig.1(G)]. The data reveal a clear difference between the spin-up and spin-down intensities of bands 1, 2 and 3, and show that bands 1 and 2 have opposite spin whereas bands 2 and 3 have the same spin (detailed analysis discussed later in text). The former observation confirms that bands 1 and 2 form a spin-orbit split pair, and the latter observation suggests that bands 2 and 3 (as opposed to bands 1 and 3) are connected above the Fermi level and form one band. This is further confirmed by directly imaging the bands through raising the chemical potential via doping [see supporting online material (APPENDIX B) [22]]. Irrelevance of bands 2 and 3 to the topology is consistent with the fact that the Fermi surface pocket they form does not enclose any  $\vec{k}_T$ . Because of a dramatic intrinsic weakening of signal intensity near crossings 4 and 5, and the small energy and momentum splittings of bands 4 and 5 lying at the resolution limit of modern spin-resolved ARPES spectrometers, no conclusive spin information about these two bands can be drawn from the methods employed in obtaining the data sets in Figs 1(G)&(H). However, whether bands 4 and 5 are both singly or doubly degenerate does not change the fact that an odd number of spin-polarized FSs enclose the  $\vec{k}_T$ , which provides evidence that  $\text{Bi}_{1-x}\text{Sb}_x$  has  $\nu_0 = 1$  and that its surface supports a non-trivial Berry's phase.

We investigated the quantum origin of topological order in this class of materials. It has been theoretically speculated that the novel topological order originates

from the parities of the electrons in pure Sb and not Bi [11,23]. It was also noted [20] that the origin of the topological effects can only be tested by measuring the spin-texture of the Sb surface, which has not been measured. Based on quantum oscillation and magneto-optical studies, the bulk band structure of Sb is known to evolve from that of insulating  $\text{Bi}_{1-x}\text{Sb}_x$  through the hole-like band at H rising above  $E_F$  and the electron-like band at L sinking below  $E_F$  [23]. The relative energy ordering of the  $L_a$  and  $L_s$  states in Sb again determines whether the surface state pair emerging from  $\bar{\Gamma}$  switches partners [Fig.2(A)] or not [Fig.2(B)] between  $\bar{\Gamma}$  and  $\bar{M}$ , and in turn determines whether they support a non-zero Berry's phase.

In a conventional spin-orbit metal such as gold, a free-electron like surface state is split into two parabolic spin-polarized sub-bands that are shifted in  $\vec{k}$ -space relative to each other [18]. Two concentric spin-polarized Fermi surfaces are created, one having an opposite sense of in-plane spin rotation from the other, that enclose  $\bar{\Gamma}$ . Such a Fermi surface arrangement, like the schematic shown in figure 2(B), does not support a non-zero Berry's phase because the  $\vec{k}_T$  are enclosed an even number of times (2 for most known materials).

However, for Sb, this is not the case. Figure 2(C) shows a spin-integrated ARPES intensity map of Sb(111) from  $\bar{\Gamma}$  to  $\bar{M}$ . By performing a systematic incident photon energy dependence study of such spectra, previously unavailable with He lamp sources [24], it is possible to identify two V-shaped surface states (SS) centered at  $\bar{\Gamma}$ , a bulk state located near  $k_x = -0.25 \text{ \AA}^{-1}$  and resonance states centered about  $k_x = 0.25 \text{ \AA}^{-1}$  and  $\bar{M}$  that are hybrid states formed by surface and bulk states [19] (APPENDIX C [22]). An examination of the ARPES intensity map of the Sb(111) surface and resonance states at  $E_F$  [Fig.2(E)] reveals that the central surface FS enclosing  $\bar{\Gamma}$  is formed by the inner V-shaped SS only. The outer

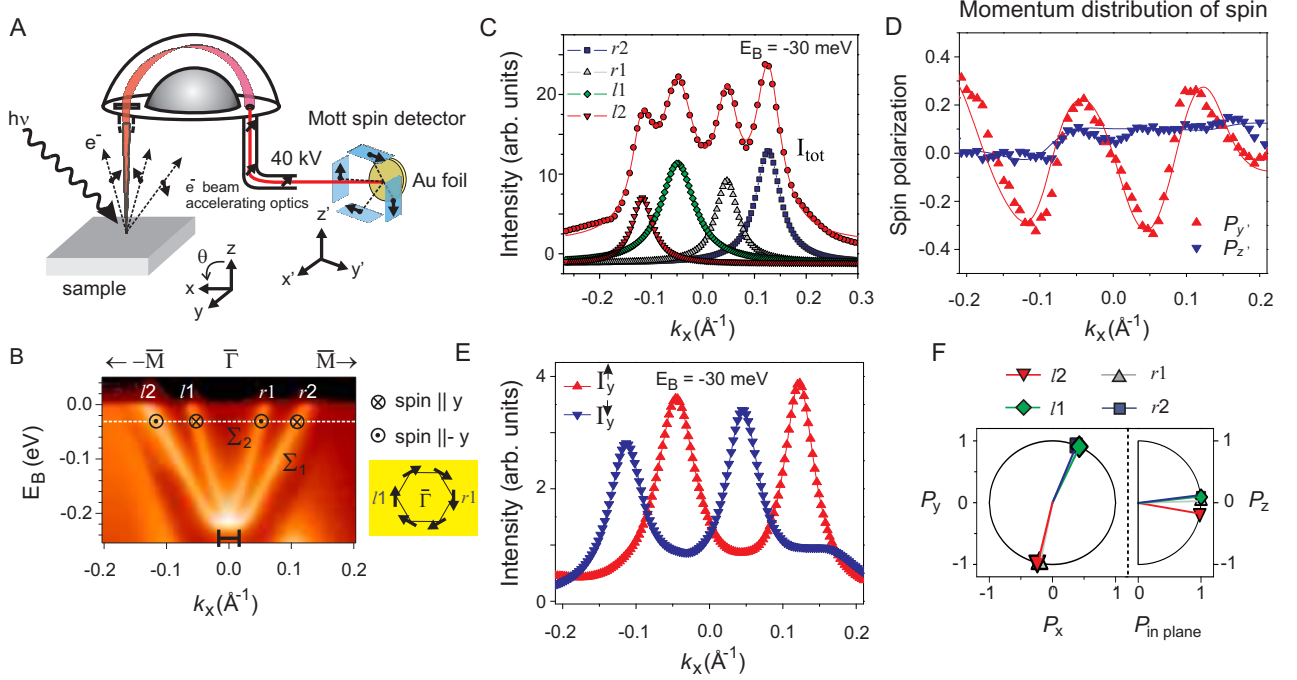


FIG. 3: Topological Spin-Texture and  $\pi$  Berry's Phase in pure Sb (Antimony)

V-shaped SS on the other hand forms part of a tear-drop shaped FS that does *not* enclose  $\bar{\Gamma}$ , unlike the case in gold. This tear-drop shaped FS is formed partly by the outer V-shaped SS and partly by the hole-like resonance state. The electron-like resonance state FS enclosing  $\bar{M}$  does not affect the determination of  $\nu_0$  because it must be doubly spin degenerate (APPENDIX D [22]). Such a FS geometry [Fig.2(G)] suggests that the V-shaped SS pair may undergo a partner switching behavior expected in Fig.2(A). This behavior is most clearly seen in a cut taken along the  $\bar{\Gamma}$ - $\bar{K}$  direction since the top of the bulk valence band is well below  $E_F$  [Fig.2(F)] showing only the inner V-shaped SS crossing  $E_F$  while the outer V-shaped SS bends back towards the bulk valence band near  $k_x = 0.1 \text{ \AA}^{-1}$  before reaching  $E_F$ . The additional support for this band dispersion behavior comes from tight binding surface calculations on Sb [Fig.2(D)], which closely match with experimental data below  $E_F$ . Our observation of a single surface band forming a FS enclosing  $\bar{\Gamma}$  suggests that pure Sb is likely described by  $\nu_0 = 1$ , and that its surface may support a Berry's phase.

Confirmation of a surface  $\pi$  Berry's phase rests critically on a measurement of the relative spin orientations (up or down) of the SS bands near  $\bar{\Gamma}$  so that the partner switching is indeed realized, which cannot be done without spin resolution. Spin resolution was achieved using a Mott polarimeter that measures two orthogonal spin components of a photoemitted electron [27,28]. These two components are along the  $y'$  and  $z'$  directions of the Mott coordinate frame, which lie predominantly in and out of the sample (111) plane respectively. Each of

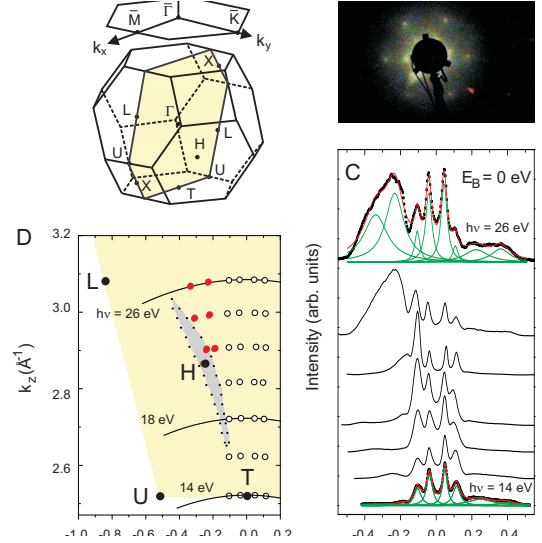


FIG. S2: Incident energy and Brillouin zone space in pure Sb crystal.

these two directions represents a normal to a scattering plane defined by the photoelectron incidence direction on a gold foil and two electron detectors mounted on either side (left and right) [Fig.3(A)]. Strong spin-orbit coupling of atomic gold is known to create an asymmetry in the scattering of a photoelectron off the gold foil that depends on its spin component normal to the scattering plane [28]. This leads to an asymmetry between the left intensity ( $I_{y',z'}^L$ ) and right intensity ( $I_{y',z'}^R$ ) given by

$A_{y',z'} = (I_{y',z'}^L - I_{y',z'}^R) / (I_{y',z'}^L + I_{y',z'}^R)$ , which is related to the spin polarization  $P_{y',z'} = (1/S_{eff}) \times A_{y',z'}$  through the Sherman function  $S_{eff} = 0.085$  [27,28]. Spin-resolved momentum distribution curve data sets of the SS bands along the  $-\bar{M}-\bar{\Gamma}-\bar{M}$  cut at  $E_B = -30$  meV [Fig.3(B)] are shown for maximal intensity. Figure 3(D) displays both  $y'$  and  $z'$  polarization components along this cut, showing clear evidence that the bands are spin polarized, with spins pointing largely in the (111) plane. In order to estimate the full 3D spin polarization vectors from a two component measurement (which is not required to prove the partner switching or the Berry's phase), we fit a model polarization curve to our data following the recent demonstration in Ref-[26], which takes the polarization directions associated with each momentum distribution curve peak [Fig.3(C)] as input parameters, with the constraint that each polarization vector has length one (in angular momentum units of  $\hbar/2$ ). Our fitted polarization vectors are displayed in the sample  $(x, y, z)$  coordinate frame [Fig.3(F)], from which we derive the spin-resolved momentum distribution curves for the spin components parallel ( $I_y^\uparrow$ ) and anti-parallel ( $I_y^\downarrow$ ) to the  $y$  direction (APPENDIX B [22]) as shown in figure 3(E). There is a clear difference in  $I_y^\uparrow$  and  $I_y^\downarrow$  at each of the four momentum distribution curve peaks indicating that the surface state bands are spin polarized [Fig.3(E)], which is possible to conclude even without a full 3D fitting. Each of the pairs  $l2/l1$  and  $r1/r2$  have opposite spin, consistent with the behavior of a spin split pair, and the spin polarization of these bands are reversed on either side of  $\bar{\Gamma}$  in accordance with the system being time reversal symmetric [ $E(\vec{k}, \uparrow) = E(-\vec{k}, \downarrow)$ ] [Fig.3(F)]. The measured spin texture of the Sb(111) surface states (Fig.3), together with the connectivity of the surface bands (Fig.2), uniquely determines its belonging to the  $\nu_0 = 1$  class. Therefore the surface of Sb carries a non-zero ( $\pi$ ) Berry's phase via the inner V-shaped band and pure Sb can be regarded as the parent metal of the  $\text{Bi}_{1-x}\text{Sb}_x$  topological insulator class, in other words, the topological order originates from the Sb wave functions.

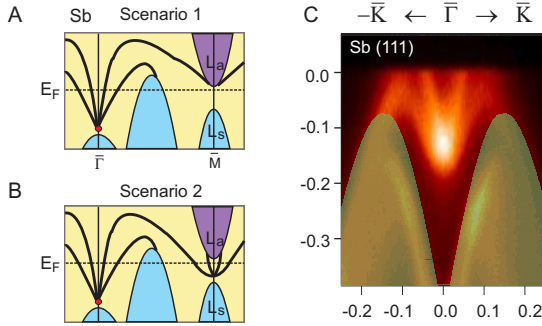


FIG. S4: Surface band topologies in pure Sb.

Our spin polarized measurement methods (Fig.1 and 3) uncover a new type of topological quantum number

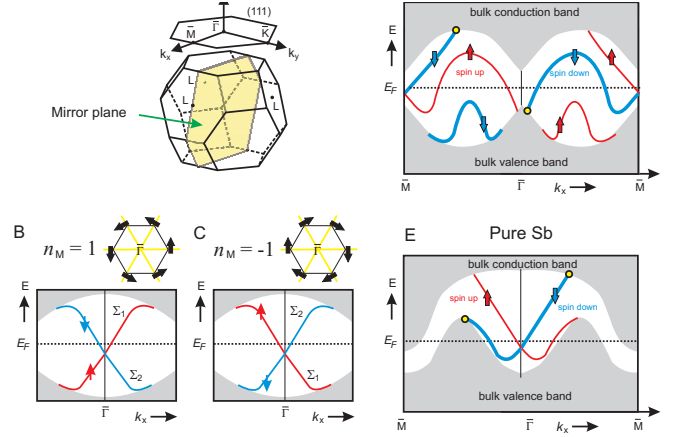


FIG. S6:  $Z_2$  Topology and Berry's Phase associated with the spin-polarized surface states in Sb and BiSb. The value of topological Mirror Chern number in Sb and BiSb suggest left-handed chirality quantum number  $n_M = -1$ .

$n_M$  which provides information about the chirality properties. Topological band theory suggests that the bulk electronic states in the mirror ( $k_y = 0$ ) plane can be classified in terms of a number  $n_M (= \pm 1)$  that describes the handedness (either left or right handed) or chirality of the surface spins which can be directly measured or seen in spin-resolved experiments [20]. We now determine the value of  $n_M$  from our data. From figure 1, it is seen that a single (one) surface band, which switches partners at  $\bar{M}$ , connects the bulk valence and conduction bands, so  $|n_M| = 1$  (APPENDIX F [22]). The sign of  $n_M$  is related to the direction of the spin polarization ( $\vec{P}$ ) of this band [20], which is constrained by mirror symmetry to point along  $\pm \hat{y}$ . Since the central electron-like FS enclosing  $\bar{\Gamma}$  intersects six mirror invariant points [see Fig.3(B)], the sign of  $n_M$  distinguishes two distinct types of handedness for this spin polarized FS. Figures 1(F) and 3 show that for both  $\text{Bi}_{1-x}\text{Sb}_x$  and Sb, the surface band that forms this electron pocket has  $\langle \vec{P} \rangle \propto -\hat{y}$  along the  $k_x$  direction, suggesting a left-handed rotation sense for the spins around this central FS thus  $n_M = -1$ . Therefore, both insulating  $\text{Bi}_{1-x}\text{Sb}_x$  and pure Sb possess equivalent chirality properties – a definite spin rotation sense (left-handed chirality, see Fig.3(B)) and a topological Berry's phase.

These spin-resolved experimental measurements reveal an intimate and straightforward connection between the topological numbers ( $\nu_0, n_M$ ) and the physical observables. The  $\nu_0$  determines whether the surface electrons support a non-trivial Berry's phase, and if they do, the  $n_M$  determines the spin handedness of the Fermi surface that manifests this Berry's phase. The 2D Berry's phase is a critical signature of topological order and is not realizable in isolated 2D electron systems, nor on the surfaces of conventional spin-orbit or exchange coupled magnetic materials. A non-zero Berry's phase is known, theoretically, to protect an electron system against the almost

universal weak-localization behavior in their low temperature transport [11,13] and is expected to form the key element for fault-tolerant computation schemes [13,29], because the Berry's phase is a geometrical agent or mechanism for protection against quantum decoherence [30]. Its remarkable realization on the  $\text{Bi}_{1-x}\text{Sb}_x$  surface represents an unprecedented example of a 2D  $\pi$  Berry's phase, and opens the possibility for building realistic prototype systems to test quantum computing modules. In general, our results demonstrate that spin-ARPES is a powerful probe of topological order and quantum spin Hall physics, which opens up a new search front for topological materials for novel spin-devices and fault-tolerant quantum computing.

### Details of Materials and Methods

Spin-integrated angle-resolved photoemission spectroscopy (ARPES) measurements were performed with 14 to 30 eV photons on beam line 5-4 at the Stanford Synchrotron Radiation Laboratory, and with 28 to 32 eV photons on beam line 12 at the Advanced Light Source, both endstations being equipped with a Scienta hemispherical electron analyzer (see VG Scienta manufacturer website for instrument specifications). Spin-resolved ARPES measurements were performed at the SIS beam line at the Swiss Light Source using the COPHEE spectrometer (31, p.15) with a single 40 kV classical Mott detector and photon energies of 20 and 22 eV. The typical energy and momentum resolution was 15 meV and 1.5% of the surface Brillouin zone (BZ) respectively at beam line 5-4, 9 meV and 1% of the surface BZ respectively at beam line 12, and 80 meV and 3% of the surface BZ respectively at SIS using a pass energy of 3 eV. The undoped and Te doped  $\text{Bi}_{1-x}\text{Sb}_x$  single crystal samples were each cleaved from a boule grown from a stoichiometric mixture of high purity elements. The boule was cooled from 650 to 270 °C over a period of 5 days and was annealed for 7 days at 270 °C. Our ARPES results were reproducible over many different sample batches. Determination of the Sb compositions in  $\text{Bi}_{1-x}\text{Sb}_x$  to 1% precision was achieved by bulk resistivity measurements, which are very sensitive to Sb concentration (23), as well as scanning electron microscopy analysis on a cleaved surface showing lateral compositional homogeneity over the length scale of our ARPES photon beam size. X-ray diffraction (XRD) measurements were used to check that the samples were single phase, and confirmed that the single crystals presented in this paper have rhombohedral A7 crystal structure (point group  $R\bar{3}m$ ). The XRD patterns of the cleaved crystals exhibit only the (333), (666), and (999) peaks showing that the naturally cleaved surface is oriented along the trigonal

(111) axis. Room temperature data were recorded on a Bruker D8 diffractometer using Cu  $K\alpha$  radiation ( $\lambda=1.54 \text{ \AA}$ ) and a diffracted beam monochromator. The in-plane crystal orientation was determined by Laue x-ray diffraction prior to insertion into an ultra high vacuum environment. Cleaving these samples *in situ* between 10 K and 55 K at chamber pressures less than  $5 \times 10^{-11}$  torr resulted in shiny flat surfaces, characterized *in situ* by low energy electron diffraction (LEED) to be clean and well ordered with the same symmetry as the bulk [Fig. S2(B)]. This is consistent with photoelectron diffraction measurements that show no substantial structural relaxation of the Sb(111) surface (32).

### Methods of using incident photon energy modulated ARPES to separate the bulk from surface electronic states of pure antimony (Sb)

In this section we detail incident photon energy modulated ARPES experiments on the low lying electronic states of single crystal Sb(111), which we employ to isolate the surface from bulk-like electronic bands over the entire BZ. Figure S2(C) shows momentum distributions curves (MDCs) of electrons emitted at  $E_F$  as a function of  $k_x$  ( $\parallel \bar{\Gamma}\bar{M}$ ) for Sb(111). The out-of-plane component of the momentum  $k_z$  was calculated for different incident photon energies ( $h\nu$ ) using the free electron final state approximation with an experimentally determined inner potential of 14.5 eV (37, 38). There are four peaks in the MDCs centered about  $\bar{\Gamma}$  that show no dispersion along  $k_z$  and have narrow widths of  $\Delta k_x \approx 0.03 \text{ \AA}^{-1}$ . These are attributed to surface states and are similar to those that appear in Sb(111) thin films (37). As  $h\nu$  is increased beyond 20 eV, a broad peak appears at  $k_x \approx -0.2 \text{ \AA}^{-1}$ , outside the  $k$  range of the surface states near  $\bar{\Gamma}$ , and eventually splits into two peaks. Such a strong  $k_z$  dispersion, together with a broadened linewidth ( $\Delta k_x \approx 0.12 \text{ \AA}^{-1}$ ), is indicative of bulk band behavior, and indeed these MDC peaks trace out a Fermi surface [Fig. S2(D)] that is similar in shape to the hole pocket calculated for bulk Sb near H (36). Therefore by choosing an appropriate photon energy (e.g.  $\leq 20$  eV), the ARPES spectrum at  $E_F$  along  $\bar{\Gamma}\bar{M}$  will have contributions from only the surface states. The small bulk electron pocket centered at L is not accessed using the photon energy range we employed [Fig. S2(D)].

Now we describe the experimental procedure used to distinguish pure surface states from resonant states on Sb(111) through their spectral signatures. ARPES spectra along  $\bar{\Gamma}\bar{M}$  taken at three different photon energies are shown in Fig. ???. Near  $\bar{\Gamma}$  there are two rather linearly dispersive electron like bands that meet exactly at  $\bar{\Gamma}$  at a binding energy  $E_B \sim -0.2$  eV. This behavior is consistent with a pair of spin-split surface bands that become degenerate at the time reversal invariant momentum ( $\vec{k}_T$ )  $\bar{\Gamma}$  due to Kramers degeneracy. The surface origin of this pair of bands is established by their

lack of dependence on  $h\nu$  [Fig. ??(A)-(C)]. A strongly photon energy dispersive hole like band is clearly seen on the negative  $k_x$  side of the surface Kramers pair, which crosses  $E_F$  for  $h\nu = 24$  eV and gives rise to the bulk hole Fermi surface near H [Fig. S2(D)]. For  $h\nu \leq 20$  eV, this band shows clear back folding near  $E_B \approx -0.2$  eV indicating that it has completely sunk below  $E_F$ . Further evidence for its bulk origin comes from its close match to band calculations [Fig. S2(D)]. Interestingly, at photon energies such as 18 eV where the bulk bands are far below  $E_F$ , there remains a uniform envelope of weak spectral intensity near  $E_F$  in the shape of the bulk hole pocket seen with  $h\nu = 24$  eV photons, which is symmetric about  $\bar{\Gamma}$ . This envelope does not change shape with  $h\nu$  suggesting that it is of surface origin. Due to its weak intensity relative to states at higher binding energy, these features cannot be easily seen in the energy distribution curves (EDCs) in Fig. ??(A)-(C), but can be clearly observed in the MDCs shown in Fig. S2(C) especially on the positive  $k_x$  side. Centered about the  $\bar{M}$  point, we also observe a crescent shaped envelope of weak intensity that does not disperse with  $k_z$  [Fig. ??(D)-(F)], pointing to its surface origin. Unlike the sharp surface states near  $\bar{\Gamma}$ , the peaks in the EDCs of the feature near  $\bar{M}$  are much broader ( $\Delta E \sim 80$  meV) than the spectrometer resolution (15 meV). The origin of this diffuse ARPES signal is not due to surface structural disorder because if that were the case, electrons at  $\bar{\Gamma}$  should be even more severely scattered from defects than those at  $\bar{M}$ . In fact, the occurrence of both sharp and diffuse surface states originates from a  $k$  dependent coupling to the bulk. As seen in Fig.2(D) of the main text, the spin-split Kramers pair near  $\bar{\Gamma}$  lie completely within the gap of the projected bulk bands near  $E_F$  attesting to their purely surface character. In contrast, the weak diffuse hole like band centered near  $k_x = 0.3 \text{ \AA}^{-1}$  and electron like band centered near  $k_x = 0.8 \text{ \AA}^{-1}$  lie completely within the projected bulk valence and conduction bands respectively, and thus their ARPES spectra exhibit the expected lifetime broadening due to coupling with the underlying bulk continuum (39).

### Method of counting spin Fermi surface $\vec{k}_T$ enclosures in pure Sb

In this section we give a detailed explanation of why the surface Fermi contours of Sb(111) that overlap with the projected bulk Fermi surfaces can be neglected when determining the  $\nu_0$  class of the material. Although the Fermi surface formed by the surface resonance near  $\bar{M}$  encloses the  $\vec{k}_T$   $\bar{M}$ , we will show that this Fermi surface will only contribute an even number of enclosures and thus not alter the overall evenness or oddness of  $\vec{k}_T$  enclosures. Consider some time reversal symmetric perturbation that lifts the bulk conduction  $L_a$  band completely above  $E_F$

so that there is a direct excitation gap at L. Since this perturbation preserves the energy ordering of the  $L_a$  and  $L_s$  states, it does not change the  $\nu_0$  class. At the same time, the weakly surface bound electrons at  $\bar{M}$  can evolve in one of two ways. In one case, this surface band can also be pushed up in energy by the perturbation such that it remains completely inside the projected bulk conduction band [Fig. S4(A)]. In this case there is no more density of states at  $E_F$  around  $\bar{M}$ . Alternatively the surface band can remain below  $E_F$  so as to form a pure surface state residing in the projected bulk gap. However by Kramers theorem, this SS must be doubly spin degenerate at  $\bar{M}$  and its FS must therefore enclose  $\bar{M}$  twice [Fig. S4(B)]. In determining  $\nu_0$  for semi-metallic Sb(111), one can therefore neglect all segments of the FS that lie within the projected areas of the bulk FS [Fig.2(G) of main text] because they can only contribute an even number of FS enclosures, which does not change the modulo 2 sum of  $\vec{k}_T$  enclosures.

In order to further experimentally confirm the topologically non-trivial surface band dispersion shown in figures 2(C) and (D) of the main text, we show ARPES intensity maps of Sb(111) along the  $-\bar{K}-\bar{\Gamma}-\bar{K}$  direction. Figure S4(C) shows that the inner V-shaped band that was observed along the  $-\bar{M}-\bar{\Gamma}-\bar{M}$  direction retains its V-shape along the  $-\bar{K}-\bar{\Gamma}-\bar{K}$  direction and continues to cross the Fermi level, which is expected since it forms the central hexagonal Fermi surface. On the other hand, the outer V-shaped band that was observed along the  $-\bar{M}-\bar{\Gamma}-\bar{M}$  direction no longer crosses the Fermi level along the  $-\bar{K}-\bar{\Gamma}-\bar{K}$  direction, instead folding back below the Fermi level around  $k_y = 0.1 \text{ \AA}^{-1}$  and merging with the bulk valence band [Fig. S4(C)]. This confirms that it is the  $\Sigma_{1(2)}$  band starting from  $\bar{\Gamma}$  that connects to the bulk valence (conduction) band, in agreement with the calculations shown in figure 2(D) of the main text.

### Investigation of the robustness of Sb spin states under random field perturbations introduced by Bi substitutional disorder

The predicted topological protection of the surface states of Sb implies that their metallicity cannot be destroyed by weak time reversal symmetric perturbations. In order to test the robustness of the measured gapless surface states of Sb, we introduce such a perturbation by randomly substituting Bi into the Sb crystal matrix (APPENDIX A). Another motivation for performing such an experiment is that the formalism developed by Fu and Kane (41) to calculate the  $Z_2$  topological invariants relies on inversion symmetry being present in the bulk crystal, which they assumed to hold true even in the random alloy  $\text{Bi}_{1-x}\text{Sb}_x$ . However, this formalism is simply a device for simplifying the calculation and the non-trivial  $\nu_0 = 1$  topological class of  $\text{Bi}_{1-x}\text{Sb}_x$  is predicted to hold true even in the absence of inversion symmetry in the bulk crystal (41). Therefore introducing

light Bi substitutional disorder into the Sb matrix is also a method to examine the effects of alloying disorder and possible breakdown of bulk inversion symmetry on the surface states of Sb(111). We have performed spin-integrated ARPES measurements on single crystals of the random alloy  $\text{Sb}_{0.9}\text{Bi}_{0.1}$ . Figure ?? shows that both the surface band dispersion along  $\bar{\Gamma}$ - $\bar{M}$  as well as the surface state Fermi surface retain the same form as that observed in Sb(111), and therefore the ‘topological

metal’ surface state of Sb(111) fully survives the alloy disorder. Since Bi alloying is seen to only affect the band structure of Sb weakly, it is reasonable to assume that the topological order is preserved between Sb and  $\text{Bi}_{0.91}\text{Sb}_{0.09}$  as we observed.

- 
- [1] N. W. Ashcroft, N. D. Mermin, *Solid State Physics* (Holt, Rinehart and Winston, New York, 1976).
- [2] K. v. Klitzing, G. Dorda, M. Pepper, *Phys. Rev. Lett.* **45**, 494 (1980).
- [3] R. B. Laughlin, *Phys. Rev. Lett.* **50**, 1395 (1983).
- [4] X. -G. Wen, *Int. J. Mod. Phys. B* **4**, 239 (1990).
- [5] D. J. Thouless *et al.*, *Phys. Rev. Lett.* **49**, 405 (1982).
- [6] J. E. Avron, D. Osadchy, R. Seiler, *Phys. Today* **56** (8), 38 (2003).
- [7] M. König *et al.*, *Science* **318**, 766 (2007).
- [8] B. A. Bernevig, T. L. Hughes, S. -C. Zhang, *Science* **314**, 1757 (2006).
- [9] N. Nagaosa, *Science* **318**, 758 (2007).
- [10] D. Hsieh *et al.*, *Nature* **452**, 970 (2008).
- [11] L. Fu, C. L. Kane, *Phys. Rev. B* **76**, 045302 (2007).
- [12] X. -L. Qi, T. Hughes, S. -C. Zhang, *Phys. Rev. B* **78**, 195424 (2008).
- [13] L. Fu, C. L. Kane, *Phys. Rev. Lett.* **100**, 096407 (2008).
- [14] C. L. Kane, E. J. Mele, *Phys. Rev. Lett.* **95**, 146802 (2005).
- [15] J. E. Moore, L. Balents, *Phys. Rev. B* **75**, 121306(R) (2007).
- [16] J. J. Sakurai, *Modern Quantum Mechanics* (Addison-Wesley, New York, 1994).
- [17] M. V. Berry, *Proc. R. Soc. London Ser. A* **392**, 45 (1984).
- [18] M. Hoesch *et al.*, *Phys. Rev. B* **69**, 241401(R) (2004).
- [19] S. Hufner, *Photoelectron Spectroscopy* (Springer-. verlag, Berlin, 1995).
- [20] J. C. Y. Teo, L. Fu, C. L. Kane, *Phys. Rev. B* **78**, 045426 (2008).
- [21] T. Hirahara *et al.*, *Phys. Rev. B* **76**, 153305 (2007).
- [22] Materials and methods, including details of sample characterization, data analysis and theoretical background, are available as supporting material on *Science Online*.
- [23] B. Lenoir *et al.*, *Fifteenth International Conference on Thermoelectrics*, 1-13 (1996).
- [24] K. Sugawara *et al.*, *Phys. Rev. Lett.* **96**, 046411 (2006).
- [25] Y. Liu, E. Allen, *Phys. Rev. B* **52**, 1566 (1995).
- [26] F. Meier *et al.*, *Phys. Rev. B* **77**, 165431 (2008).
- [27] M. Hoesch *et al.*, *J. Electron Spectrosc. Relat. Phenom.* **124**, 263 (2002).
- [28] T. J. Gay, F. B. Dunning, *Rev. Sci. Instrum.* **63**, 1635 (1992).
- [29] P. J. Leek *et al.*, *Science* **318**, 1889 (2007).
- [30] A. Kitaev, *Ann. Phys. (NY)* **303**, 2 (2003).
- [31] M. Hoesch, PhD dissertation, University of Zürich, (2002).
- [32] S. Bengió *et al.*, *Surface Science* **601**, 2908 (2007).
- [33] P. D. Johnson. *Rep. Prog. Phys.* **60**, 1217 (1997).
- [34] T. Hirahara *et al.*, *Phys. Rev.* **B76**, 153305 (2007).
- [35] D. M. Brown, S. J. Silverman, *Phys. Rev.* **136**, A290 (1964).
- [36] L. M. Falicov, P. J. Lin, *Phys. Rev.* **141**, 562 (1965).
- [37] H. Höchst, C. R. Ast, *J. Electron Spectrosc. Relat. Phenom.* **137**, 441 (2004).
- [38] X. Gonze *et al.*, *Phys. Rev.* **B44**, 11023 (1991).
- [39] E. Kneedler, K. E. Smith, D. Skelton, S. D. Kevan, *Phys. Rev.* **B44**, 8233 (1991).
- [40] Yu. M. Koroteev *et al.*, *Phys. Rev. Lett.* **93**, 046403 (2004).
- [41] L. Fu, C. L. Kane, *Phys. Rev.* **B76**, 045302 (2007).
- [42] J. C. Y. Teo, L. Fu, C. L. Kane, *Phys. Rev.* **B78**, 045426 (2008).

**FIG. 1. Theoretical spin spectrum of a topological insulator and spin-resolved spectroscopy results.** (A) Schematic sketches of the bulk Brillouin zone (BZ) and (111) surface BZ of the  $\text{Bi}_{1-x}\text{Sb}_x$  crystal series. The high symmetry points ( $\bar{L}, \bar{H}, \bar{T}, \bar{\Gamma}, \bar{M}, \bar{K}$ ) are identified. (B) Schematic of Fermi surface pockets formed by the surface states (SS) of a topological insulator that carries a Berry's phase. (C) Partner switching band structure topology: Schematic of spin-polarized SS dispersion and connectivity between  $\bar{\Gamma}$  and  $\bar{M}$  required to realize the FS pockets shown in panel-(B).  $L_a$  and  $L_s$  label bulk states at  $L$  that are antisymmetric and symmetric respectively under a parity transformation (see text). (D) Spin-integrated ARPES intensity map of the SS of  $\text{Bi}_{0.91}\text{Sb}_{0.09}$  at  $E_F$ . Arrows point in the measured direction of the spin. (E) High resolution ARPES intensity map of the SS at  $E_F$  that enclose the  $\bar{M}_1$  and  $\bar{M}_2$  points. Corresponding band dispersion (second derivative images) are shown below. The left right asymmetry of the band dispersions are due to the slight offset of the alignment from the  $\bar{\Gamma}$ - $\bar{M}_1$  ( $\bar{M}_2$ ) direction. (F) Surface band dispersion image along the  $\bar{\Gamma}$ - $\bar{M}$  direction showing five Fermi level crossings. The intensity of bands 4,5 is scaled up for clarity (the dashed white lines are guides to the eye). The schematic projection of the bulk valence and conduction bands are shown in shaded blue and purple areas. (G) Spin-resolved momentum distribution curves presented at  $E_B = -25$  meV showing single spin degeneracy of bands at 1, 2 and 3. Spin up and down correspond to spin pointing along the  $+\hat{y}$  and  $-\hat{y}$  direction respectively. (H) Schematic of the spin-polarized surface FS observed in our experiments. It is consistent with a  $\nu_0 = 1$  topology (compare (B) and (H)).

**FIG. 2. Topological character of pure Sb revealed on the (111) surface states.** Schematic of the bulk band structure (shaded areas) and surface band structure (red and blue lines) of Sb near  $E_F$  for a (A) topologically non-trivial and (B) topological trivial (gold-like) case, together with their corresponding surface Fermi surfaces are shown. (C) Spin-integrated ARPES spectrum of Sb(111) along the  $\bar{\Gamma}$ - $\bar{M}$  direction. The surface states are denoted by SS, bulk states by BS, and the hole-like resonance states and electron-like resonance states by hRS and  $e^-$ RS respectively. (D) Calculated surface state band structure of Sb(111) based on the methods in [20,25]. The continuum bulk energy bands are represented with pink shaded regions, and the lines show the discrete bands of a 100 layer slab. The red and blue single bands, denoted  $\Sigma_1$  and  $\Sigma_2$ , are the surface states bands with spin polarization  $\langle \vec{P} \rangle \propto +\hat{y}$  and  $\langle \vec{P} \rangle \propto -\hat{y}$  respectively. (E) ARPES intensity map of Sb(111) at  $E_F$  in the  $k_x$ - $k_y$  plane. The only one FS encircling  $\bar{\Gamma}$  seen in the data is formed by the inner V-shaped SS band seen in panel-(C) and (F). The outer V-shaped band bends back towards the bulk band best seen

in data in panel-(F). (F) ARPES spectrum of Sb(111) along the  $\bar{\Gamma}$ - $\bar{K}$  direction shows that the outer V-shaped SS band merges with the bulk band. (G) Schematic of the surface FS of Sb(111) showing the pockets formed by the surface states (unfilled) and the resonant states (blue and purple). The purely surface state Fermi pocket encloses only one Kramers degenerate point ( $\vec{k}_T$ ), namely,  $\bar{\Gamma}$  ( $=\vec{k}_T$ ), therefore consistent with the  $\nu_0 = 1$  topological classification of Sb which is different from Au (compare (B) and (G)). As discussed in the text, the hRS and  $e^-$ RS count trivially.

**FIG. 3. Spin-texture of topological surface states and chirality.** (A) Experimental geometry of the spin-resolved ARPES study. At normal emission ( $\theta = 0^\circ$ ), the sensitive  $y'$ -axis of the Mott detector is rotated by  $45^\circ$  from the sample  $\bar{\Gamma}$  to  $-\bar{M}$  ( $\parallel -\hat{x}$ ) direction, and the sensitive  $z'$ -axis of the Mott detector is parallel to the sample normal ( $\parallel \hat{z}$ ). (B) Spin-integrated ARPES spectrum of Sb(111) along the  $-\bar{M}$ - $\bar{\Gamma}$ - $\bar{M}$  direction. The momentum splitting between the band minima is indicated by the black bar and is approximately  $0.03 \text{ \AA}^{-1}$ . A schematic of the spin chirality of the central FS based on the spin-resolved ARPES results is shown on the right. (C) Momentum distribution curve of the spin averaged spectrum at  $E_B = -30$  meV (shown in (B) by white line), together with the Lorentzian peaks of the fit. (D) Measured spin polarization curves (symbols) for the detector  $y'$  and  $z'$  components together with the fitted lines using the two-step fitting routine [26]. (E) Spin-resolved spectra for the sample  $y$  component based on the fitted spin polarization curves shown in (D). Up (down) triangles represent a spin direction along the  $+$ ( $-$ ) $\hat{y}$  direction. (F) The in-plane and out-of-plane spin polarization components in the sample coordinate frame obtained from the spin polarization fit. Overall spin-resolved data and the fact that the surface band that forms the central electron pocket has  $\langle \vec{P} \rangle \propto -\hat{y}$  along the  $+k_x$  direction, as in (E), suggest a left-handed chirality (schematic in (B) and see text for details).

**Fig. S2. (A)** Schematic of the bulk BZ of Sb and its (111) surface BZ. The shaded region denotes the momentum plane in which the following ARPES spectra were measured. **(B)** LEED image of the *in situ* cleaved (111) surface exhibiting a hexagonal symmetry. **(C)** Select MDCs at  $E_F$  taken with photon energies from 14 eV to 26 eV in steps of 2 eV, taken in the  $TXLU$  momentum plane. Peak positions in the MDCs were determined by fitting to Lorentzians (green curves). **(D)** Experimental 3D bulk Fermi surface near H (red circles) and 2D surface Fermi surface near  $\bar{\Gamma}$  (open circles) projected onto the  $k_x$ - $k_z$  plane, constructed from the peak positions found in (C). The  $k_z$  values are determined using calculated constant  $h\nu$  contours (black curves) (see APPENDIX C

text). The shaded gray region is the theoretical hole Fermi surface calculated in (36).

**Fig. S4.** (A) Schematic of the surface band structure of Sb(111) under a time reversal symmetric perturbation that lifts the bulk conduction ( $L_a$ ) band above the Fermi level ( $E_F$ ). Here the surface bands near  $\bar{M}$  are also lifted completed above  $E_F$ . (B) Alternatively the surface band near  $\bar{M}$  can remain below  $E_F$  in which case it must be doubly spin degenerate at  $\bar{M}$ . (C) ARPES intensity plot of the surface states along the  $-\bar{K}-\bar{\Gamma}-\bar{K}$  direction. The shaded green regions denote the theoretical projection of the bulk valence bands, calculated using the full potential linearized augmented plane wave method using the local density approximation including the spin-orbit interaction (method described in 40). Along this direction, it is clear that the outer V-shaped surface band that was observed along the  $-\bar{M}-\bar{\Gamma}-\bar{M}$  now merges with the bulk

valence band.

**Fig. S6.** Implications of k-space mirror symmetry on the surface spin states. (A) 3D bulk Brillouin zone and the mirror plane in reciprocal space. (B) Schematic spin polarized surface state band structure for a mirror Chern number ( $n_M$ ) of +1 and (C) -1. Spin up and down mean parallel and anti-parallel to  $\hat{y}$  respectively. The upper (lower) shaded gray region corresponds to the projected bulk conduction (valence) band. The hexagons are schematic spin polarized surface Fermi surfaces for different  $n_M$ , with yellow lines denoting the mirror planes. (D) Schematic representation of surface state band structure of insulating  $\text{Bi}_{1-x}\text{Sb}_x$  and (E) semi metallic Sb both showing a  $n_M = -1$  topology. Yellow circles indicate where the spin down band (bold) connects the bulk valence and conduction bands.